Stability and bearing capacity of arch-shaped corrugated shell elements: experimental and numerical study

A. PIEKARCZUK[1*], K. MALOWANY[2], P. WIĘCH[1], M. KUJAWIŃSKA[2], and P. SULIK[1]

[1] Building Research Institute, 1 Filtrowa St., 00-611 Warsaw, Poland
[2] Institute of Micromechanics and Photonics, Warsaw University of Technology, 8 Św. A. Boboli St., 02-525 Warsaw, Poland

Abstract. The paper presents problems related to the numerical modeling of profiled steel sheets used as self-supporting arch structures for roof covering. The rules of preparing and full analysis of a set of numerical models of these elements with a different level of complexity are given. The models are evaluated by comparing numerical results with the results of extended experimental tests performed by 3D Digital Image Correlation (DIC) method. For each model the comparison of numerical and experimental results has been made for samples of a single-wave trapezoidal profile with corrugated web and lower flanges subjected to compression and bending. The full-field analysis allows to determine the allowed simplification of numerical models which do not affect in significant way the reliability of the results. The proposed methodology is the first step in the development of full assessment methodology for different types of self-supporting arch structures produced by ABM technology.

Key words: ABM technology, arch-shaped corrugated steel structure, FEM model, digital image correlation, data processing.

1. Introduction

Self supporting arch structures made of steel sheets were initially adopted as temporary agricultural and military structures, usually erected in countries with climate that exclude or limit in significant way load caused by wind and snow in winter season. They gained significant popularity in these applications, mainly because of low cost and short time of erection in comparison with traditional steel, timber or reinforced concrete structures. Nowadays this type of structers is increasingly often adopted as public facilities in middle and eastern European countries. The components of these structures are manufactured directly on building site using mobile production unit. First, single-wave trapezoidal profile is cold-shaped from a 0.7–1.5 mm thick coiled steel sheet (Fig. 1, stage 1). After that, the curvature of a desired radius (from 6 to 30 m) is obtained by means of appropriate corrugation of profile (Fig. 1, stage 2). The ABM 240 (Automatic Building Machine) system [1] creates profile with characteristic corrugation on web and lower flanges. The profiles are connected to each other by means of cold pressing of seams situated at the edges of upper flanges.

The considered structures are of simply supported circular arch type, subjected to dead, technological [3] and environmental loads (the latter consists of snow [4] and wind [5] action). These loads induce in the cross-section of a profile internal forces such as compression, bending and shearing. As the considered structure due to the thickness and slenderness of its web and flanges falls into the 4-th category of cross-section acc. to EN 1993-1-1 [6] standard, the structural failure is triggered with local buckling of profiles walls. Additionally, due to the compressive forces, global loss of stability of whole arch also has to be taken into account.
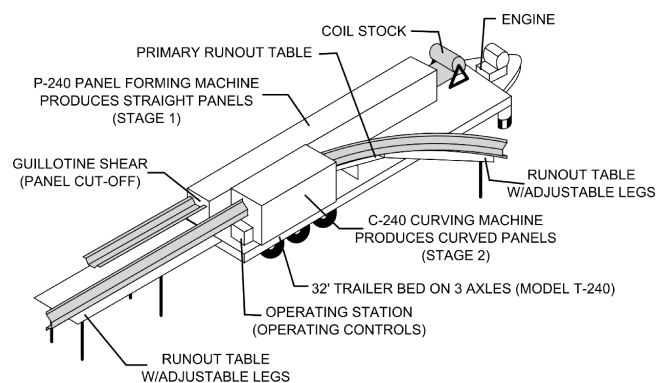

Fig. 1. The scheme of the process of cold shaping of a single profile performed at ABM 240 system (Ref. 2)

The bases for the design of the thin-walled self supporting structures are given in EN 1993-1-3 [7] and PN-B-03207:2002 [8] standards. The general rules for calculations of stability and load carrying capacity are covered by these documents. The author of the work [9] gives valuable advises concerning the application of [7] and [8] standards in engineering practice. He also stresses the importance of taking into account geometrical and physical nonlinearities and suggests that numerical analysis could be the efficient solution to this problem. However due to the corrugation of profile walls these methods prove to be insufficient and leading to overestimation of both its stiffness and ultimate load. The other reliable methods of design of such structures are also non-existent at the moment.

The influence of corrugation depth and radius of curvature of profiles on their mechanical properties has been discussed in [1, 11]. The shape of cross section investigated in [11] varies from the one considered in our paper, but the analysis of the results obtained from numerical calculations and

---

*e-mail: a.piekarczuk@itb.pl

standard [10] gives the valuable insight into the limitations of the latter. It showed satisfying correlation for plain-walled profile; however that was not a case for a curved profile with corrugated wall. This confirms the limitations of standard [10] design method in the case of considered structures.

The mode of local stability loss of corrugated profiles subjected to axial and eccentric compression loads had been investigated in paper [12]. The results of numerical calculations and experimental tests had been compared and they showed discrepancies in critical load value ranging from 8% to 24%. However in this work the axial and compression stiffness of tested profiles had not been taken into account.

The initial works concerning stability and load carrying capacity of self-supporting arch structures made of profiled steel sheets have been also made in Building Research Institute. The test of a full scale model of arch consisting of 4 trapezoid profiles of 12 m span and 6 m radius and its numerical evaluation was a subject of paper [13]. The simplified distribution of internal forces assumed in this paper (simulating a uniform snow load) is shown in Fig. 2. The variability of direction of bending moment and its ratio to compressive load across the arch span is clearly visible. The failure mode of the structure consists of local buckling and loss of load carrying capacity as well as global loss of an arch stability. The exact order of occurrence of these incidents depends on many factors such as the arch curvature, its slenderness, cross-section geometry, mechanical properties of utilized material, load distribution etc. According to EN 1993-1-1 [6] slenderness of cross section walls corresponds to the 4th class section. In such case it is assumed that if load level corresponding to local buckling of cross-section walls is approached the effective width of the walls is reduced. As a result the neutral axis is shifted, bending and axial stiffness reduced and consequently load distribution affected. These factors result in the emergence of local instability. The compressive loads simultaneously cause the global buckling of whole arch structure.
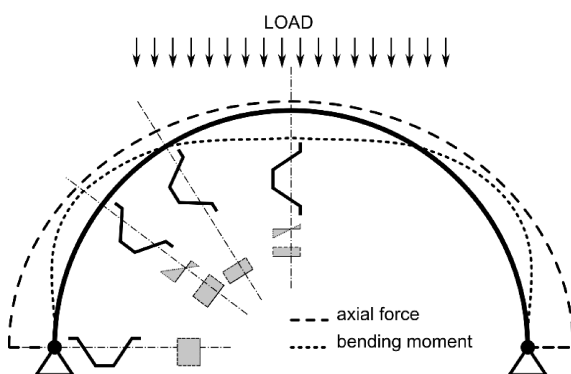

Fig. 2. Simplified distribution of internal loads

During the tests significant nonlinear behavior of the structure had been observed. For experimental tests 3D Digital Image Correlation method had been applied and it has been proved that it is well suited and extremely helpful to perform full field monitoring and measurement of displacement maps during experiments. The comparison of the results obtained from calculation and experiment showed that the mode of global loss of stability is significantly influenced by local buckling. It was also shown that the failure occurs in sudden manner and is not signaled with significant increase in an arch displacement. The applied numerical model has been assumed as being capable of only coarse estimation of an ultimate load and insufficient for displacement calculation.

This was mainly caused by the corrugations and waves occurring in the profiles produced by ABM 240 system, which make code calculation methods largely inadequate. Satisfying analytical models of such structures are currently unavailable, while the existing ones do not describethe mechanism of local loss of stability in sufficient way.In the structural analysis identification of an actual failure mechanism is of uttermost importance. The interpretation of full-scale tests is difficult due to the insufficient control of applied load, problems with prediction of failure location and resulting limitations to quality of measurements. The coexistence of global buckling phenomena further impairs usefulness of such tests results. All these facts provide motivation to perform systematic studies of the problem starting from analysis of a test specimen consisting of a profile section of a limited length which can be considered as sufficient for the purpose of investigation of load carrying capacity and local buckling of profile. Such a specimen can be subjected to load acting with known eccentricity in an attempt to simulate interaction between axial load and bending moment that occurs in an arch structure. The short length of the specimen allows observation of failure mode on a limited area and suppress global buckling influence. Based on the previous positive experience [12] the 3D DIC method has been applied for the purpose of measurement of displacement and strain fields. Obtained data are intended to be used for the purpose of validation of an arch section numerical model. The finally chosen numerical model would be used for prediction of failure mode, ultimate load and stiffness of an arch section and it is going to be applied for analysis of sections with various curvature radius, sheet thickness, load eccentricity. Thus, the numerical models would substitute experimental tests greatly decreasing their number and form a basis for the evaluation of the entire range of products.

In the paper we at first present the methodology of the laboratory tests including the description of samples, loading conditions and 3D Digital Image Correlation method. Next three numerical models of the loaded sample with different level of its simplification are introduced and the results of stress and displacement calculations are compared. Finally the numerical results obtained for different FEM models are compared with point-wise and full-field experimental results in order to gain more knowledge and verify numerical models.

2. Experimental methodology

2.1. Test sample. The tests have been performed with 1.0 m long sample of a profile of 18 m curvature radius (Fig. 3). The relatively short sample was chosen to exclude the influence of global loss of stability. The sample has been made of S355

grade steel sheet of 1.4 mm nominal thickness. Initial location of the neutral axis X and Y has been calculated without taking into account the influence of corrugation of profile walls. Take a note that the actual neutral axis Y is shifted in the direction of upper flange. The actual dimensions of the sample have been included in Table 1. The meanings of symbols used in the table are explained in Fig. 3.
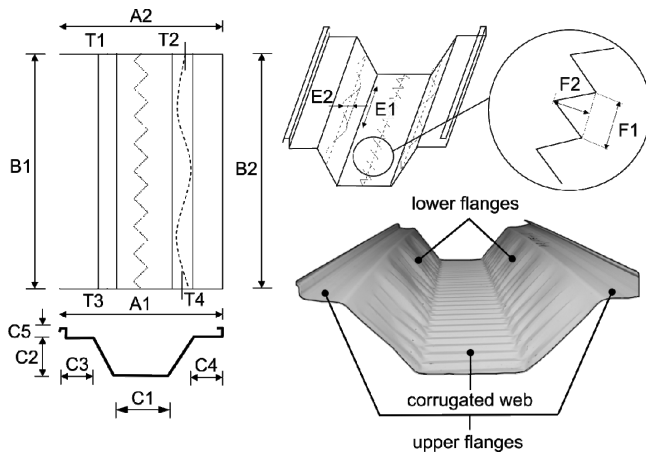

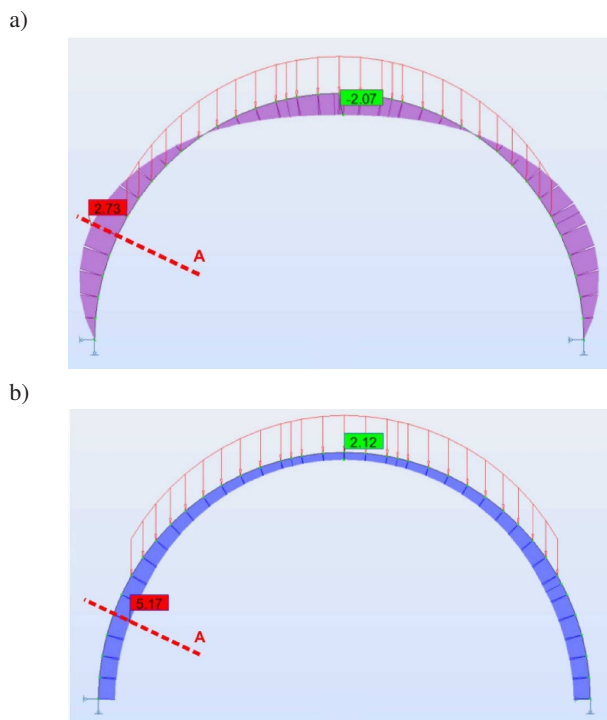Fig. 3. The sample view and explanation of the symbols used in Table 1

a)

b)

Fig. 4. Example diagrams of the internal forces:a) bending moment and b)axial force

The load system selected for the experiments enables simultaneous compression and bending section. A set of loads causes compressive stress in the web section. Such a system guarantees an extreme load stress at the most vulnerable to loss of stability site. Figure 4 shows the diagrams of bending moment and axial force resulting from linear snow load. The dashed line represents the greatest place bending moments and longitudinal forces.

In the section A bending causes compression of the web in municipal occurrence corrugating, additionally there is a compressive force directed along the longitudinal axis. To capture a clear effect of the local loss of stability, it is assumed that the axial force acts on the eccentricity $e = 105$ mm which corresponds to the position of force compression on the web corrugated profile.

The load scheme and location of the sample at the loading rig is shown in Fig. 5.
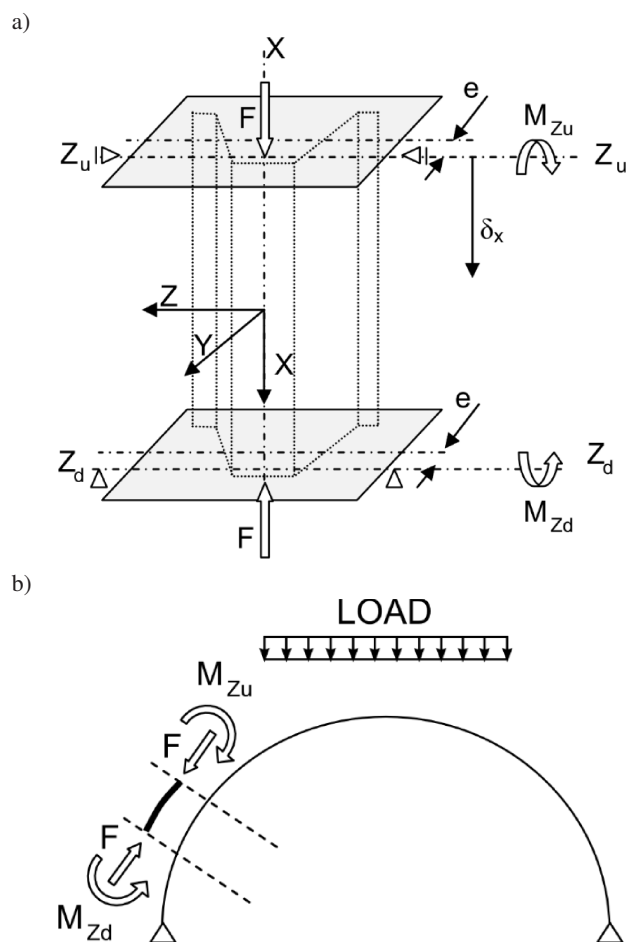
a)

b)

Fig. 5. Diagram of the support and load: a) the terms and conditions of load and support research, b) representation conditions

Table 1
Actual dimensions of the sample (all values are given in mm)

Width and height of web and flanges									Depth and length of the wave		Depth and length of corrugation		Sheet thickness			
A1	A2	B1	B2	C1	C2	C3	C4	C5	E1	E2	F1	F2	T1	T2	T3	T4
696	675	1016	1016	201.7	160.9	80.0	87.5	27.3	204.7	11.4	33.8	2.2	1.38	1.37	1.38	1.37

A. Piekarczuk, K. Malowany, P. Więch, M. Kujawińska, and P. Sulik

Actual values of tensile strength and yield stress of sample material have been obtained from the tensile tests made accordingly to standard ISO 6892-1 [14]. 30 samples have been tested, with average values of $R_{p0.2}$ and R_m being 337 MPa (yield point) and 388 MPa (tensile strenght) respectively.

2.2. Test bench. The main purpose of the tests was to establish the profile load carrying capacity as well as the relationship between load and deformation. It was assumed from the beginning that test bench has to fulfill the following requirements:

- limitation of a failure mode to local buckling,
- prevention of deplanation of the sample's support zones,
- elimination of any loads other than axial despite any sample deformation during the test.

A test sample is placed between the rigid plates. The axis of rotation extends along the load device and is off set by the value of eccentricity. The top plate is able to move along the axis of $\delta(X)$ and rotation of both plates with respect to Z_u and Z_d axes is also allowed. Figure 5 shows the load and support scheme at the test bench and its representation in the full-size element.

On the basis of the above assumptions a prototype test rig had been built. The schematic view and the photo of the test set-up are shown in Fig. 6.
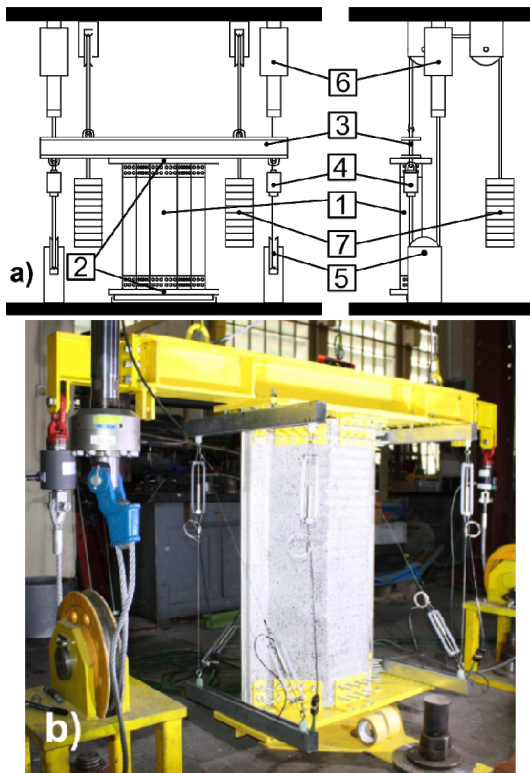

Fig. 6. The experimental set-up: a) the scheme of the rig and b) the photo of the sample at the test bench

The setup deplanation has been prevented by rigid steel plates (pos. 2) fastened to the sample (pos. 1) by means of

number of bolts. Lower plate has been standing on a support allowing its rotation in one direction. I-beam (pos. 3) has been attached to upper plate. Counterweights (pos. 7) attached to this beam via ropes and pulleys kept sample in upright position. Load has been applied by means of pulleys (pos. 5) and ropes attached to the same I-beam (pos. 2) as counterweights were.

Except of an axial load it is possible for limited amount of torsional moment to occur only. However the measurements made during the tests shown that the torsional deformation of a sample and any moment induced by it is negligible up to the moment of the sample's failure. Friction during the test is limited to rotational degree of freedom of lower support only and it was reduced by applying of graphite-molybdenum lubricant. The load has been measured by the strain gauge transducers (pos. 4) and, due to the application of PID controlled hydraulic actuators (pos. 6), it maintained the same value for both tendons during the tests. The value of eccentricity of an applied load can be changed in 15 mm increments.

2.3. DIC set-up and data analysis. Due to the complicated geometry of corrugated, thin walled profiles the preparation of numerical model is significantly error-prone. Thus DIC method has been used during the tests as it gives reliable information about the actual buckling modes that are important for the verification of FE model. DIC is a non-coherent light based method which enables full-field measurements of shape, displacements, and strains [15, 16]. The two-dimensional version of DIC (2D DIC) measurement consists of the acquisition of a series of images of a tested object before and after load (or during loading), over a certain Area of Interest (AOI). The surface of the measured object needs to have random texture which is in our case applied within the AOI by spraying black paint (dotted pattern) at the white paint background. One of the images serves as a reference for the others (deformed). The reference image is divided into small rectangular regions (subsets) consisting of $N \times N$ pixels. Dimensions of subsets are dependent on the quality of the random pattern. The DIC algorithm is then tracking the position of each subset from the reference image in all other subsequent images, using the maximum zero-mean normalized sum of squared difference function criterion (or any other correlation metric). The location of the center point of the most similar subset found in a deformed image defines the in-plane displacement vector (u_x denotes displacements in 'x' axis and u_z denotes displacements in 'z' axis; Fig. 7a). Repeating this process over the AOI provide a displacement map, that is sampled as defined by the separation of adjacent subsets (step size). The 3D DIC is a technique, which combines the 2D DIC with stereovision, by using two cameras for observation of the same AOI, it is possible to obtain the 3D shape of the surface of an object and measure out-of plane displacements (u_y denotes displacements in 'y' axis), however the out-of-plane measurement error is larger than the in-plane one, and strongly depends on a stereo angle [17, 18]. According to [15] minimum displacement error can be less than 0.001 pixels, indicated by data post-processing. However, it must be highlight that in real ap-

plications the accuracy of measurements strongly depends on such factors as image noise and stability of experimental condition. Strains (ε_{xx}, ε_{zz} – strains along x and z coordinates) are calculated from displacements [15, 19] using equations:

$$\varepsilon_{xx} = \frac{\partial u}{\partial x} + \frac{1}{2}\left[\left(\frac{\partial u}{\partial x}\right)^2 + \left(\frac{\partial w}{\partial x}\right)^2\right],$$

$$\varepsilon_{zz} = \frac{\partial w}{\partial z} + \frac{1}{2}\left[\left(\frac{\partial u}{\partial z}\right)^2 + \left(\frac{\partial w}{\partial z}\right)^2\right]. \tag{1}$$

It is worthwhile to note that the DIC 3D method is working in full-field and in experimental test provides much more data than point wise techniques. The measurements are carried out in thousands or millions of points of the measured object simultaneously and in three directions. The measurements of the sample were performed with the 3D DIC system which comprises of two AVT Pike F-1600 (4872×3248 pixels) monochromatic cameras equipped with 28 mm lenses, set on an angle of 30° and pointing to the same AOI at the specimen (Fig. 7b,c). Before performing the experiment, the system was calibrated with utilization of the commercial software VIC 3D [20]. Standard deviation of the residuals projection errors for 24 views of the calibration target and from both cameras was 0.058 pixel. Distortions of the 28 mm lenses were included in the calibration process. The setup was mounted on aluminum frame to enable easy modification and mobility. In order to ensure sufficient lighting, two 200 W LED lamps (13 000 lumen) equipped with a light diffuser ('soft box') were used. The capture of images by both cameras was synchronized and pairs of frames were collected every 2 seconds during 300 seconds of the experiment. The Field of View (FOV) of the systemwas 1.5×1 m, so it was well fitted to the size of the samples.
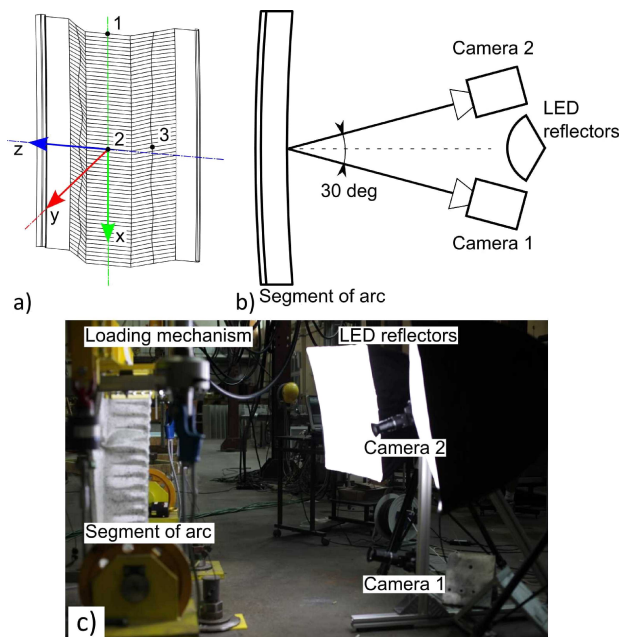

Fig. 7. The experimental system: a) orientation of coordinate system and location of three points adopted for further analysis; b) scheme and c) photo of measurement system based on 3D DIC

The displacements and strain maps were calculated with the Vic3D software [20]. The quality of data and resulting accuracy of measurements at a given point was determined by the confidence interval for match at points within the Area of Interest and it is given by sigma value in pixels (Fig. 8a). The range of sigma for maximum load was 0–0.3 pixel. This values after scaling based on 3D DIC system parameters provided the estimate of the acuracy of displacement measurements for ±0.01 mm. The maximum values of sigma (low level of confidence) were located at the bending edges of the sample (incl. the peaks of the corrugation). The results of measurements are not displayed at these points as can be seen at the shape map shown in Fig. 8b, where data at several locations are incomplete (white spots).
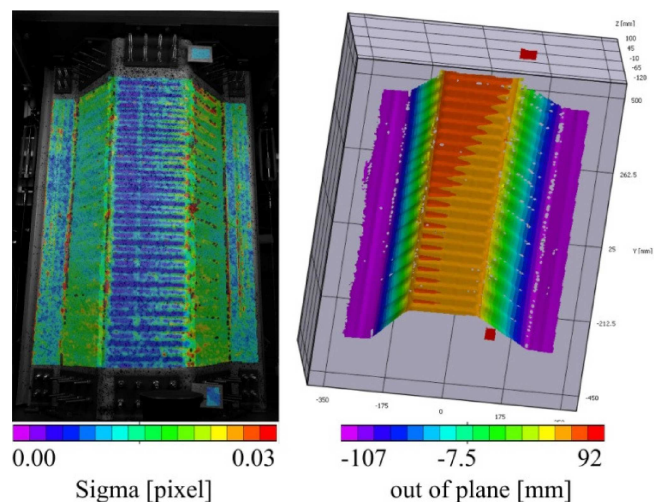

Fig. 8. Example results of measurement: a) the map of sigma – confidence interval for the match at the points within AOI, and b) the shape of measured segment of arch

3. Numerical models and their analysis

Numerical models have been created with Ansys Finite Element Method software. Three different models have been prepared, each with different degree of simplifications of geometrical properties. All models have the same 18 m curvature radius, 1 m length and were based on actual geometry of the tested sample included in Table 1. In order to simulate accurately the experimental conditions, the assumed boundary conditions (Fig. 9) allowed: movement of upper edge in the direction of the force load and rotation of both (upper and lower) edges around z axis only.

Both upper and lower edges have been modeled as rigid by means of multiple point constrains (so called "remote support" in Ansys software). All nodes belonging to the given edge stay in a plane and the initial shape of the edge is preserved during deformation. Both upper and lower plane can move during deformation, in the direction of unconstrained degrees of freedom. Thus, according to Fig. 9, the plane including upper edge can be translated in x axis direction and rotated with respect to z axis ($X_1 \neq 0$ and $R_{z1} \neq 0$). The

plane including lower edge is only permitted to rotate with respect to z axis ($R_{z2} \neq 0$).
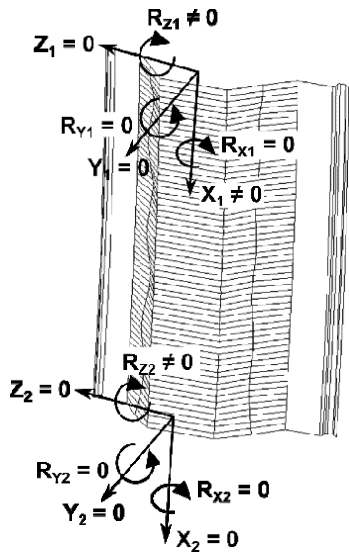

Fig. 9. Boundary conditions of upper and lower edges of the modeled sample, with local coordination systems.

Non-linear stress analysis accounting for material and geometrical nonlinearities has been made. Bilinear material model have been assumed on a basis of $R_{p0,2}$ and R_m values obtained from the tests. Newton-Raphson method of nonlinear analysis has been applied and influence of large displacement taken into account. The S281 general purpose quadratic 4-sided shell element with 8 nodes and 6 degree of freedom in each node has been chosen. The node numbering and the direction of the normal to the surface are shown in Fig. 10.
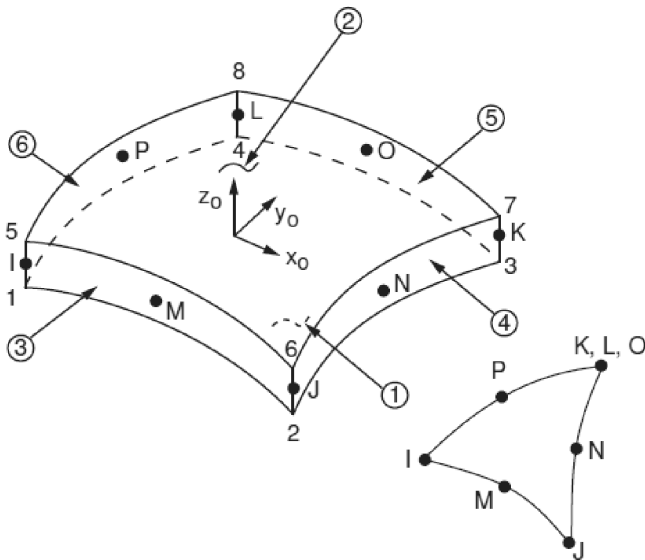

Fig. 10. The Ansys S281 shell element

Three numerical models, with the geometries shown in Fig. 11, were considered. The first model is the simplest one, omitting corrugations and wave-like disturbance in lower flanges shapes. In the second model corrugation of web and

lower flanges have been taken into account and in the third model wave-shaped disturbance have been added to the webs.
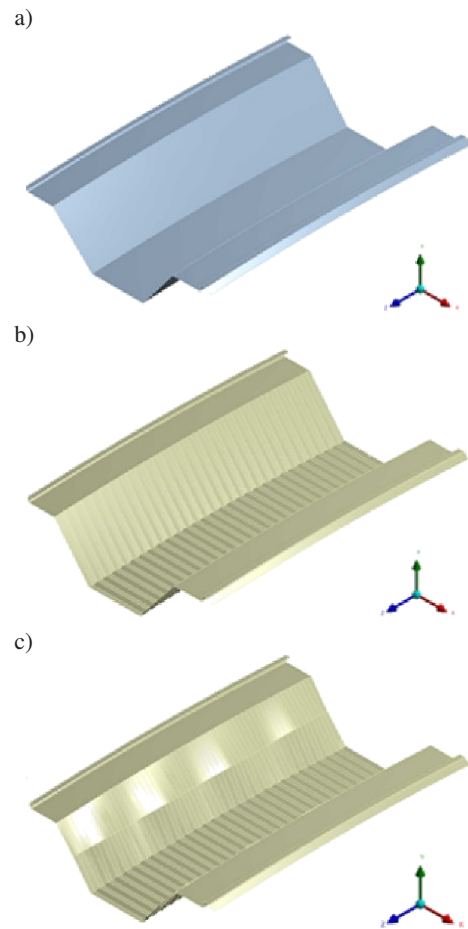

Fig. 11. The geometry of numerical models: a) planar model (1st), b) corrugation model (2nd) and c) corrugation and wavy model (3rd)

To compare the behaviour of all three models, the calculations of inter alia maps of equivalent von Mises stresses and total displacements for the ultimate load (according to Table 2)had been performed and the respective maps of both quantities are presented in Figs. 12 and 13.
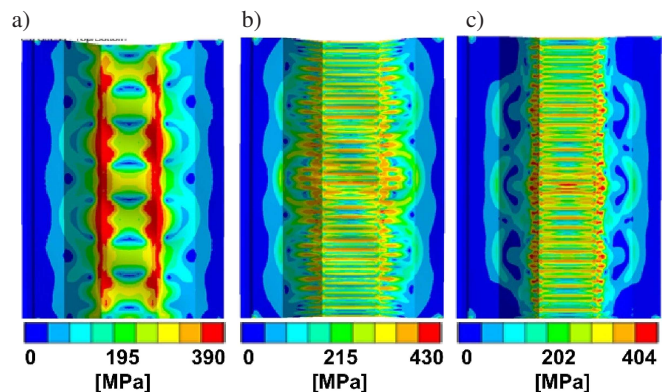

Fig. 12. The maps of equivalent von Mises stress at the ultimate load for: a) 1st model, b) 2nd model and c) 3rd model

a)   b)   c)

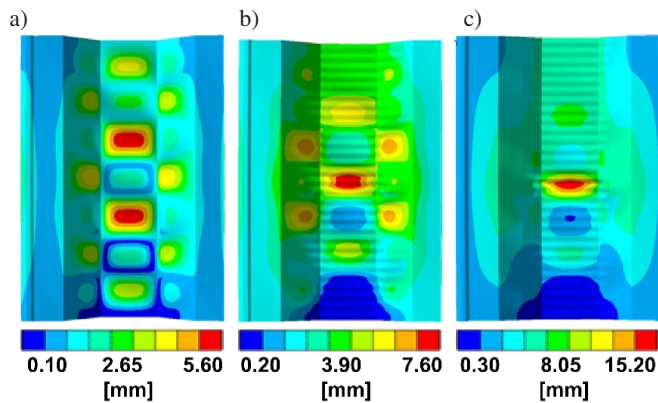| 0.10 | 2.65 | 5.60 | 0.20 | 3.90 | 7.60 | 0.30 | 8.05 | 15.20 |

[mm]   [mm]   [mm]

Fig. 13. The maps of total displacement at the ultimate load for: a) 1st model, b) 2nd model and c) 3rd model

It is clear, that omitting corrugations increase the stiffness of lower flanges and web and shifts the neutral axis towards the middle of the cross-section height. Due to this fact, despite the identical boundary conditions in all three models, the 1st model suffers from different relationship between the axial force and resulting bending moment. In the case of 2nd and 3rd models the von Mises stress distribution is quite similar except for the webs. It should be kept in mind that the profile webs have much less significant impact on its load carrying capacity as well as on the axial and bending stiffness (for the considered direction of bending moment). Therefore it should not be of much importance if the results from the numerical model of profile section are to be implemented in the simplified beam model.

The results of calculations obtained with the 1st model again differ significantly from the two others. In the case of 1st and 2nd model the displacement maps confirms, that the differences are limited to profile webs.

4. Validation of numerical models

Validation of the numerical models is performed in two main stages. At first the comparison of the displacements u_x, u_y, and u_z in selected points of the structure in the function of load is performed between all three models and experimental data. Secondly the full-field comparison of the failure mode maps and between DIC and numerical displacement maps is provided.

4.1. Matching of experimental and numerical results. It is crucial to match properly the coordinate systems, in which the numerical and experimental results are calculated, before validation of numerical models by experimental results. It is also important to remove from experimental data the unwanted additional data connected to imperfection of experimental set-up, e.g. impact of backlash in joints.

Typically in the 3D DIC analysis the coordinate system is based on information of the initial shape of a sample. The origin of this system is located at the mass centroid of all object points, with y axis normal to the best-fit plane of the shape data [20]. In our case to match the coordinate system

we transform DIC coordinate system using the markers integrated with stochastic texture (Fig. 14a,b).

| 2.80 | 21.80 | 40.80 | -0.57 | 0.25 | 1.07 |

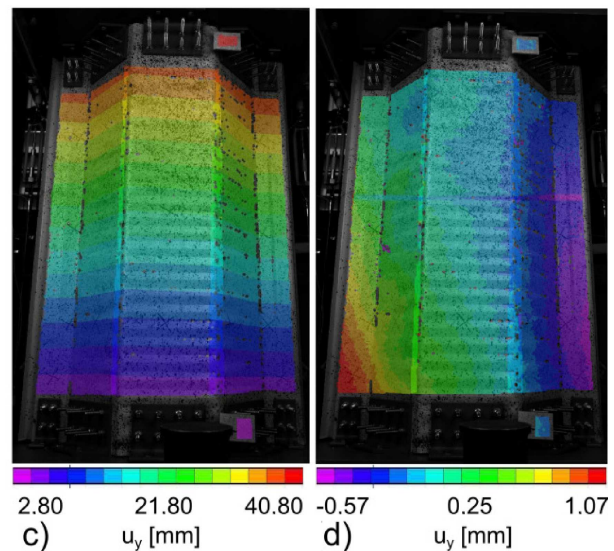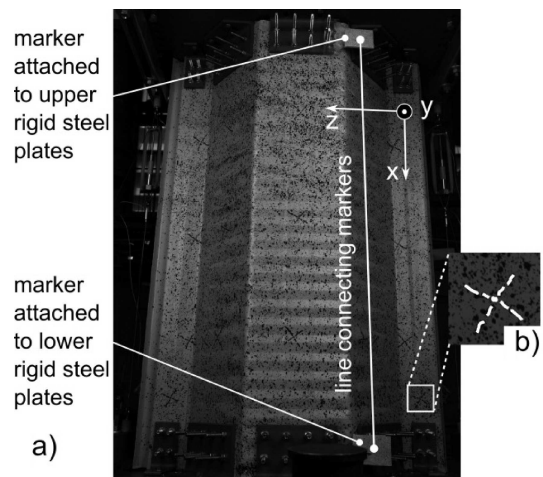c) u_y [mm]   d) u_y [mm]

Fig. 14. The principles of data post-processing: a) the image of the sample with markers' positions and line used for data post-processing operations, b) one of markers used for transformation of coordinate system; example of out of plane displacements maps for 0.6 kN force, c) before and d) after post-processing of data

Next the unwanted displacement data have to be removed. The good example of such operation is the process of backslash elimination at the first stage of applying load. The backslash resulted in random displacements (Fig. 14c) and rotations which were not allowed in numerical simulations (as discussed in Sec. 3). In order to enable comparison between numerical and experimental data the dedicated post-processing method was implemented based on transformation of the obtained displacements [21]. Using the markers attached to the rigid steel plates (Fig. 14a), the line was determined (parallel to the direction of force load). The applied transformations of displacements removed the rotations of the determined line. It should be pointed out, that the markers were not directly attached to the lower support and location of force applying, therefore rotation of determined line

around an axis z is not equivalent to R_{Z2}. In relation to the boundary condition of a numerical model (see Sec. 3), the following terms and conditions have been preserved: rotations R_{X2} & R_{Y2} were forbidden and rotations R_{Z1} & R_{Z2} were allowed. However, in experimental data in contrast to numerical model, the rotations of R_{X1} & R_{Y1} could appear, caused by uncontrolled skew of the upper rigid steel plates (Fig. 6a). The example of post-processing of out – of-plane displacement maps obtained for 0.6 kN are shown in Fig. 14c,d.

4.2. Point-wise validation of numerical models. The extreme values of u_x, u_y, and u_z displacements are observed in points 1 (located at the top of corrugated web section), 2 (located at the middle of corrugated web) and 3 (located at middle of corrugated flange) (see Fig. 7a). The points 1 and 2 concern the maximum displacement in the x and y directions, respectively. Point 3 refers to the maximum displacement of the entire sample in the z direction. This configuration of the measurement points allows for the assessment of representative movements for the entire sample. The values of these displacements obtained for all three numerical models have been compared with the experimental results. The load-displacement relationships are shown in Figs. 15–17.
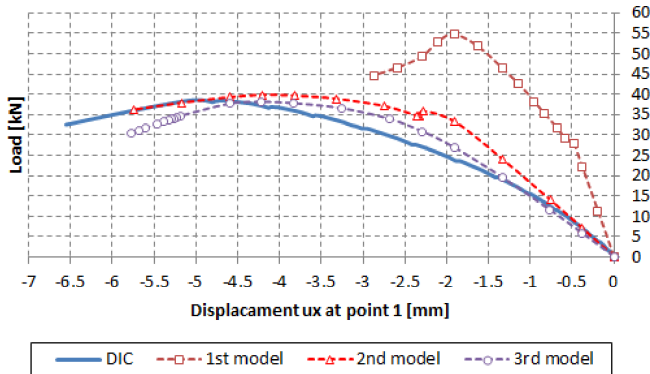

Fig. 15. The comparison of load u_x displacement functions obtained for 1st, 2nd, 3rd numerical models and experimental data (results for point 1)
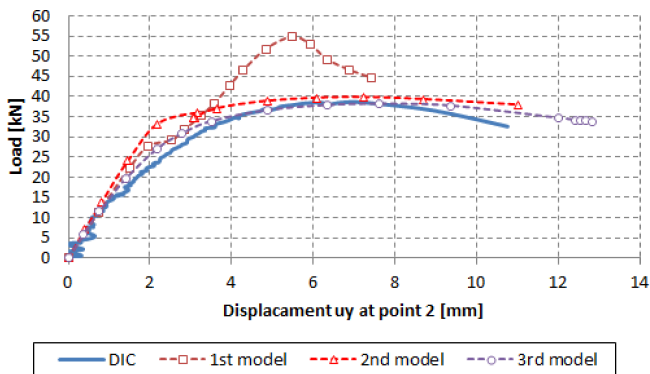

Fig. 16. The comparison of load u_y displacement functions obtained for 1st, 2nd, 3rd numerical models and experimental data (results for point 2)
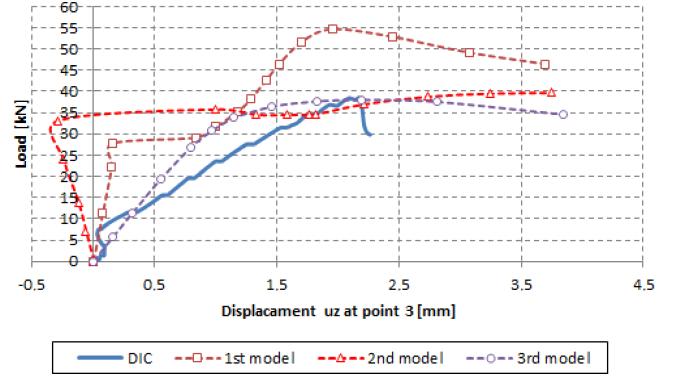

Fig. 17. The comparison of load u_z displacement functions obtained for 1st, 2nd, 3rd numerical models and experimental data (results for point 3)

The simpliest 1st model significantly overestimate both stiffness and ultimate load values. The differences between 2nd and 3rd models are less significant, particularly in case of u_x and u_y displacement. In the case of 2nd model displacements in point 3 the u_z direction still differs significantly from experimental values. This is due to the unaccounted influence of wave like disturbances of webs shape. 2nd model also still slightly overestimates load carrying capacity of the profile. The values of the displacements at ultimate load obtained from DIC and FEM models are gathered in Table 2.

Table 2
Displacements at ultimate load

	Ultimate load	Displacement at ultimate load		
	F_m [kN]	u_x [mm] at p.1	u_y [mm] at p.2	u_z [mm] at p.3
DIC experimental	38.5	−5.08	7.23	2.24
1st FEM model 1	54.7	−1.91	5.48	1.96
2nd FEM model 2	39.8	−4.20	7.23	3.75
3rd FEM model 3	38.1	−4.21	7.61	2.20

For the purpose of comparison of the results Δ_i parameter is introduced, both for the force:

$$\Delta_{Fm} = \frac{F_{DIC} - F_{FEM}}{F_{DIC}} \cdot 100 \ [\%] \qquad (2)$$

and displacement values:

$$\Delta_u = \frac{\left(F/d_{U,V,W}\right)_{DIC} - \left(F/d_{U,V,W}\right)_{FEM}}{\left(F/d_{U,V,W}\right)_{DIC}} \cdot 100 \ [\%]. \quad (3)$$

The Δ_i values for all three models are included in Table 3.

Table 3
Comparison of values of Δ_i parameters

	Ultimate load	Displacement at ultimate load		
	Δ_{Fm}	Δ_{u_x} at p.1	Δ_{u_y} at p.2	Δ_{u_z} at p.3
1st FEM model 1	−42.0%	−277%	−87.6%	−62.5%
2nd FEM model 2	−3.3%	−24.8%	−10.0%	38.4%
3rd FEM model 3	1.1%	−19.2%	6.0%	1%

The results obtained without taking into account corrugations and wave-like disturbance in webs shape differ from the experimental results to the level which prevent practical application of 1st model. Unfortunately this level of model simplification is used in a design process quite often, leading both to the overestimation of ultimate loads and incorrect load distribution along an arch. 2nd model with corrugated lower flanges and web gives acceptable estimation of ultimate load, u_x and u_y values. The displacement u_z differ significantly (38%) from the experimental value. Including additional disturbance of webs shape in 3rd model decrease the error in calculated u_z value, but the quality of the other results remains in affected in significant way.

The corrugation of web and lower flanges of a profile can be seen as a form of geometrical imperfections, determining the mode of failure. It was observed that without the corrugation the numerical model exhibits poor convergence requiring greater number of load steps in an analysis and greater computing power. This is especially true in the case, when initial deformations taken from buckling analysis are not applied to the model. This drawback can be however at least partially offseted by potentially less number of elements required to sufficient description of a simplified geometry.

Beside displacements, the strains in the vicinity of point 2 have been investigated with 3rd model. In Fig. 18 the relationship between load and strains in directions perpendicular and parallel to longitudinal axis of profile (that is ε_{zz} and ε_{xx} respectively).
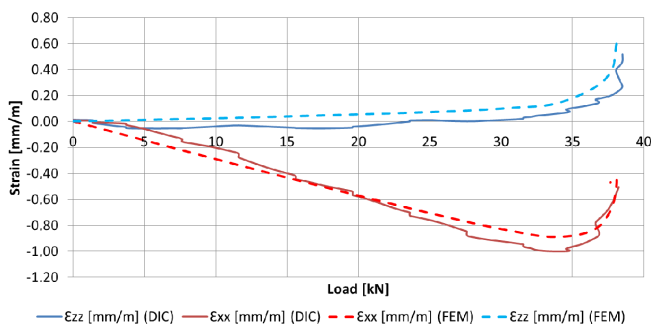

Fig. 18. Comparison of strains in point 2 vicinity (FEM results for 3rd model)

The difference between strain values obtained from DIC and FEM 3rd model varies from 2% to 20%, depending on load level. It should be noted, that due to the corrugated surface values of ε_{xx} strains exhibit large variability from point to point. Therefore it is necessary to carefully select areas both for DIC and FEM model used for the integration of ε_{xx} values intended for comparison. In x direction this area should cover length of a single corrugation to obtain the useful results and cause "smear" of corrugation. This effect is of course much less pronounced in the case of ε_{yy} strain values.

4.3. Full-field validation of numerical models. The good way to check qualitatively the correctness of a model is to compare numerical and experimetal failure mode maps. As shown in Fig. 19 the photo of the experimental failure region

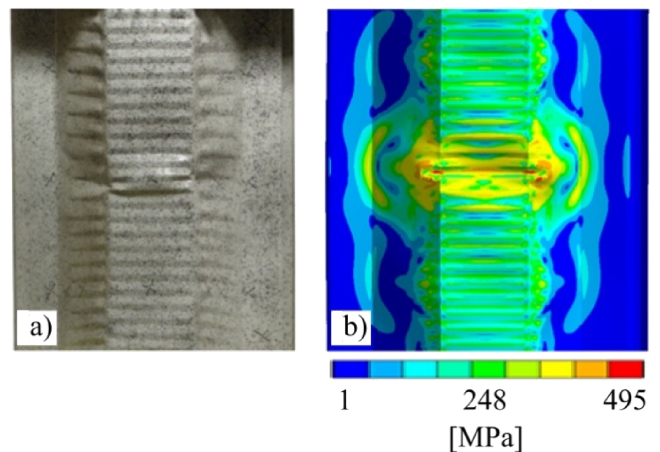is in very good agreement with the failure mode map obtained for the 3rd model.

Fig. 19. The failure mode maps obtained from: a) experiment (photo) and b) 3rd model

In order to perform full-field quantitative comparison, the displacements maps u_x, u_y, and u_z obtained from DIC and numerical analysis, are shown respectively in Figs. 20–22.
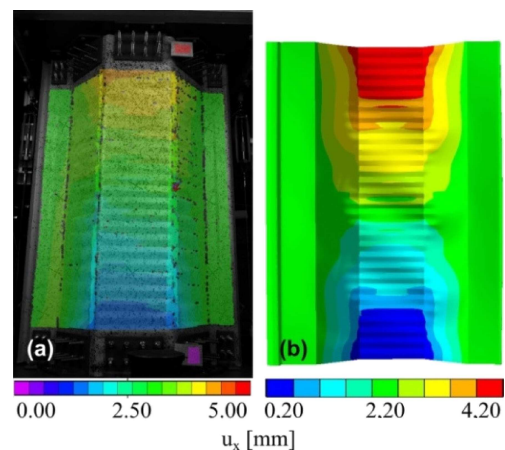

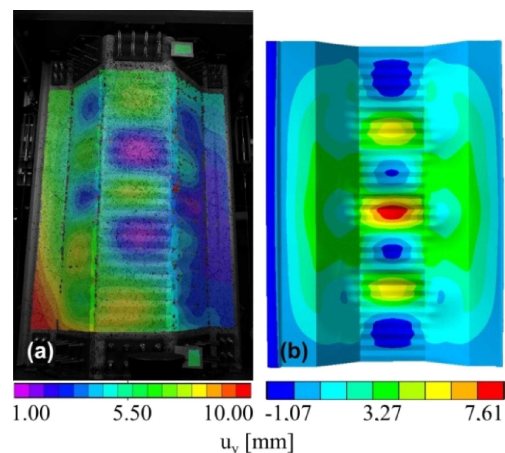Fig. 20. The displacement u_x obtained from: a) experiment and b) 3rd model

Fig. 21. The displacement u_y obtained from: a) experiment and b) 3rd model
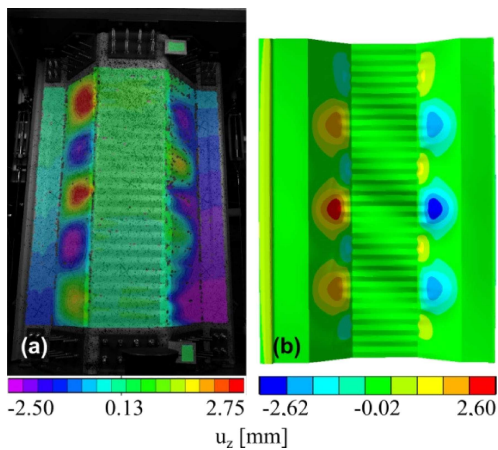
Fig. 22. The displacement u_z obtained from: a) experiment and b) 3rd model

The displacement maps u_x, u_y, and u_z obtained from the calculations show good convergence in both: the character and values with the test results. In some cases (Figs. 21, 22) slight disturbances of displacement maps obtained with DIC method can be observed. This is caused by unavoidable deviations in the specimen geometry and support conditions (e.g. connected with precision of assembly). This minor disturbances have insignificant influence on the final results and conclusions.

5. Conclusions and further research

The simplest way of modelling of a profile geometry which omits its corrugations and other disturbances of the shape leads to highly overestimated value of ultimate load as well, as highly underestimated values of displacements. These errors occur despite the fact that for the simplified model geometry, the physical and geometric nonlinear effects have been taken into account for the calculations. Unfortunately this level of profile geometry simplification is most frequently used for practical calculations, as it represents the highest detailing of profile geometry that can be directly incorporated in a numerical model of whole arch structure without increasing demand for computing power beyond reasonable level.

The most complicated third model and the second model which omits wave-like disturbances of web shape only, give results close to the experimental ones. If the effects of displacements in z direction are unimportant for the further analysis, the level of geometry details of second model can be seen as optimal with respect to both to quality of results and work consumption. However, if this is not the case, the implementation of all measurable geometrical properties is necessary, like it was made in the case of the third model. Unfortunately both levels of geometry description details are not applicable directly in a numerical model of whole arc structure and require additional analysis steps.

The unique properties of 3D DIC method implemented for the experimental tests allows precise observation of failure mode and enables measurement of displacement values

in locations, that could be otherwise difficult to access for traditional displacement sensors. DIC method also decrease risk of improper placement of sensors, no matter whether it is caused by improper assumptions or unexpected behavior of a specimen and test equipment. The importance of this is easy to see when reading i.e. paper [12]. The placement of the dial gauges during the tests described in [12] requires particularly careful preliminary numerical analysis. Any deviation from the predicted buckling form can have detrimental impact on the measured values and cause misleading conclusions.

In future, the already validated numerical model is going to be used for the estimation of ultimate axial load, ultimate bending moment envelope as well, as flexural and axial stiffness given in terms of axial load and bending moment values. These are going to be implemented in 2-D FEM model utilizing beam elements. It will make possible to perform static calculations of whole structure with computing power available in modern PC grade hardware. The proposed methodology is the first step in the development of full assessment methodology for different types of self-supporting arch structures produced by ABM technology.

REFERENCES

[1] R. Walentyński, R. Cybulski, and K. Kozieł, "Numericalmodels of ABM K-span steel arch panels", *Architecture Civil Engineering Environment* 4, 105–114 (2011).
[2] US Navy Course, *Steel Builder*, NAVEDTRA 14251, 2 (1996).
[3] EN 1991-1-1 Eurocode 1: "Actions on structures – Part 1–1: General actions – Densities, self-weight, imposed loads for buildings".
[4] EN 1991-1-3 Eurocode 1: "Actions on structures – Part 1–3: General actions – Snow loads".
[5] EN 1991-1-4 Eurocode 1:"Actions on structures – Part 1–4: General actions – Wind action".
[6] EN 1993-1-1 Eurokode 3: "Design of steel structure. General rules and rules for buildings".
[7] EN 1993-1-3 Eurokode 3: "Design of steel structure. General rules – Supplementary rules for cold-formed members and sheeting".
[8] PN-B-03207:2002 "Steel structures. Structures of cold formed thin gauge members and sheeting. Design and execution".
[9] A. Biegus, "The static-strength analysis of arc corrugated sheets", *Steel Structures. Scientific andTechnicalSection* 7, 24–28 (2003).
[10] EN 1993-1-5Eurokode 3, "Design of steel structures. General rules - plated structural elements".
[11] R. Walentyński, M. Cybulska, and R. Cybulski, "Influence of geometrical imperfrctions on the local stability of thin – walled elements",*Steel Structures. Theory and Applications* 3, 105–113 (2014).
[12] Li-Li Wu, Xuan-Neng Gao, Young-Jiu Shi, and Yuan-Qing Wang, "Theoretical and experimental study on interactive local

buckling of arch-shaped corrungated steel roof", *Steel Structures* 6, 45–54 (2006).

[13] A. Piekarczuk, M. Malesa, M. Kujawinska, and K. Malowany, "Application of hybrid FEM-DIC method for assessment of low cost building structures", *Experimental Mechanics* 52 (9), 1297–1311 (2012).

[14] ISO 6892-1, "Metallic materials – Tensile testing – Part 1: Method of test at room temperature".

[15] M. Sutton, J-J. Orteu, and H. Schreier, *Image Correlation for Shape, Motion and Deformation Measurements. Basic Concepts, Theory and Applications*, Springer, New York, 2009.

[16] B. Pan, "Recent progress in digital image correlation", *Experimental Mechanics* 51 (7), 1223–1235 (2011).

[17] Y.-Q. Wang, M. A.Sutton, X.-D. Ke, and H.W. Schreier, "Error propagation in stereo vision: Part I: Theoretical developments", *Experimental Mechanics* 51 (4), 405–422 (2011).

[18] X.-D. Ke, H.W. Schreier, M.A. Sutton, and Y.-Q. Wang, "Error propagation in stereo vision: Part II: Experimental validation", *Experimental Mechanics* 51 (4), 423–441 (2011).

[19] T.C. Chu, W.F. Ranson, M.A. Sutton, and W.H. Peters, "Applications of digital-image-correlation techniques to experimental mechanics", *Experimental Mechanics* 25 (3), 232–244 (1985).

[20] http://www.correlatedsolutions.com (01.10.2014).

[21] M. Malesa and M. Kujawińska, "Deformation measurements by digital image correlation with automatic merging of data distributed in time", *Applied Optics* 52 (19), 4681–4692 (2013).